Transient and steady state magneto-optical studies of the CsPbBr₃ crystal

Uyen N. Huynh ●,[1] Teddy Feng,[2] Dipak Raj Khanal,[1] Haoliang Liu,[1] Paul Bailey,[1]
Rikard Bodin,[1] Peter C. Sercel ●,[3] Jinsong Huang ●,[2] and Z. Valy Vardeny[1,*]

[1]*Department of Physics and Astronomy, University of Utah, Salt Lake City, Utah 84112, USA*
[2]*Department of Applied Physical Sciences, University of North Carolina at Chapel Hill, North Carolina 27599, USA*
[3]*Center for Hybrid Organic Inorganic Semiconductors for Energy, Golden, Colorado 80401, USA*

We have studied the magneto-optical properties of photoexcitations in CsPbBr₃ single crystal using the technique of picosecond time-resolved quantum beatings (QBs) in the circularly polarized photoinduced reflection as well as steady state magnetocircular dichroism (MCD) in CsPbBr₃ film. In the Voigt geometry at magnetic field strength $B > 0$, we observed fast and slow QB oscillations that we attribute to the Larmor precession frequency of electrons and holes, respectively. From the linear frequency dependence on B, we extract the carrier anisotropic Landé g factors for applied **B** along [010] and [001]; for electrons $|g^e_{[001]}| = 1.95 \pm 0.04$ and $|g^e_{[010]}| = 1.82 \pm 0.04$, whereas for holes $|g^h_{[001]}| = 0.69 \pm 0.02$ and $|g^h_{[010]}| = 0.76 \pm 0.02$. These values are in excellent agreement with a **k·p** model calculation applied to CsPbBr₃. Surprisingly, at $B = 0$, we still observed QB oscillation of ∼500 MHz that we interpret as due to the Overhauser field that originates from the spin-aligned nuclei caused by the Knight field. From the measured MCD spectrum vs B, we obtained the g factor of the bright excitons $g_{ex} = 2.18 \pm 0.08$ showing that the g value of holes in CsPbBr₃ is positive. We also measured the temperature and magnetic field dependencies of the electron and hole spin dephasing times which support the Elliot-Yafet spin-relaxation mechanism.

I. INTRODUCTION

The hybrid organic-inorganic trihalide perovskite (HOIP) semiconductors have been intensively studied, driven by their excellent optoelectronic properties [1–4]. All-inorganic CsPbX_3 perovskites, where X is a halogen, have also attracted attention recently because of their better structural stability over the HOIP since the organic (MA⁺/FA⁺) cation is replaced by inorganic Cs⁺. In addition, these compounds have the advantage of solution-processable, easy-to-make crystalline thin films and optical gap tuning capability [5]. CsPbBr₃ has excellent optoelectronic properties such as strong light absorption and relatively high photoluminescence (PL) quantum yield [6,7]. CsPbBr₃ single crystals are known to have low trap density, which is several orders of magnitude lower than that of polycrystalline thin films, making them more viable for device application [8]. Previous studies of CsPbBr₃ using transient Kerr rotation have demonstrated relatively long spin relaxation time up to 5 ns at 4 K [9]. The optically induced spin polarization and quantum beatings (QBs) have been reported and attributed to separated photocarriers [9].

Here, we present a systematic investigation of the spin dynamics in a high-quality single crystal of CsPbBr₃ [8] using the technique of picosecond transient circularly polarized photoinduced reflectivity [c-PPR(t)] upon application of a magnetic field in the Voigt configuration. We have mea-sured the electron and hole spin relaxation dynamics using the method of QBs at different magnetic fields **B** and temperature T, using two crystal orientations, namely, (001) and (110). From the dependence of the QB frequency on magnetic field strength and direction, we obtained the anisotropic Landé g factors of electrons and holes, which are in excellent agreement with **k·p** calculations. Unexpectedly, we have also observed zero-field QB oscillation of ∼500 MHz along the (110) crystal facet, which we attribute as due to the Overhauser field that originates from the spin-polarized nuclei via the spin-flop process from the spin-polarized photocarriers [10–12]. We have also used the magnetic circular dichroism (MCD) spectrum of CsPbBr₃ films from which we obtained the g value of the bright excitons, in good agreement with the g values of electron and holes measured by the QB method showing that the hole g factor in CsPbBr₃ is positive.

II. EXPERIMENTAL RESULTS AND DISCUSSION

Figure 1(a) shows the absorption spectrum of thin film CsPbBr₃ measured at 50 K. The absorption spectrum is dominated by an exciton band at the lower end of the interband transition. To extract the exciton energy, we fitted the absorption spectrum using the Elliott formula equation [13,14] which includes both exciton and interband contributions. Good fit was obtained using an exciton energy $E_{exc} = 2.34$ eV and exciton binding energy $E_b = 20$ meV, which are within the accepted values mentioned in previous reports [9,15].

Figure 1(b) shows the steady state photoinduced absorption (PA) spectrum of the polycrystalline film measured at low
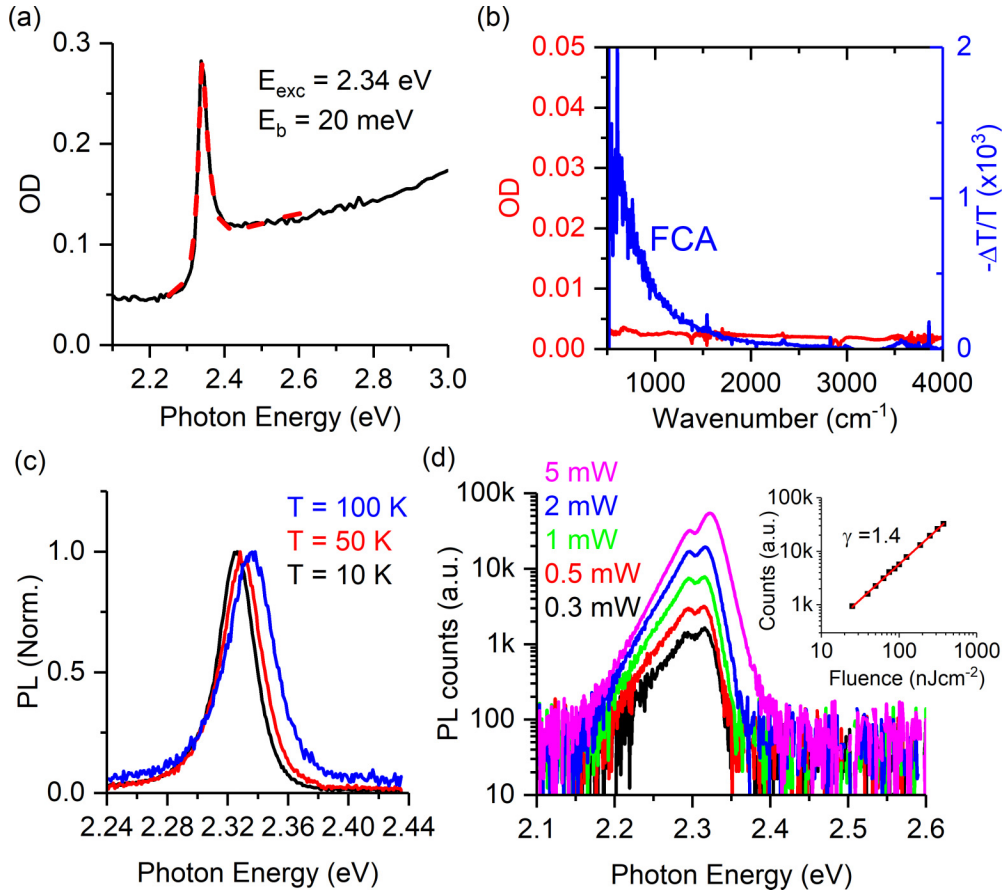
*val@physics.utah.edu

FIG. 1. (a) The absorption spectrum of CsPbBr$_3$ thin film (black line) measured at 50 K. The red dashed line is a fit using the Elliott equation [13] with exciton energy at 2.34 eV and exciton binding energy of 20 meV. (b) The absorption (red) and photoinduced absorption (PA) (blue) spectra between 500 to 4000 cm^{-1} using a Fourier-transform infrared spectrometer measured at 50 K. The PA spectrum shows free carrier absorption (FCA) < 2000 cm^{-1}. (c) The temperature dependent photoluminescence (PL) spectrum of CsPbBr$_3$ thin film excited at 447 nm with power of 0.5 mW. (d) The PL spectrum of CsPbBr$_3$ crystal measured at various excitation powers at $T = 4$ K. The inset shows the PL intensity as a function of the laser fluence in logarithmic scale and a linear fit with a slope γ of 1.4.

photon energies using a Fourier-transform infrared spectrometer, as described in Supplemental Material Sec. 1 [15]. This method shows the characteristic signature of long-lived photoexcitations. For this measurement, the sample placed in a He cryostat was photoexcited using a continuous-wave diode laser at 447 nm, and the change in the optical density due to the steady state photoexcited charged carriers was measured in the photon energy range of 500−4000 cm^{-1} using the light from a glow bar. As seen, the PA spectrum exhibits an absorption band <4000 cm^{-1} which we assigned to free carrier absorption because of the ω^{-2} spectrum. From the PA value at 1000 cm^{-1} [optical density (OD) ~ 0.01], we estimate the steady state photoexcited carrier density to be $\sim 10^{18}$ cm^{-3}, which is large enough to charge most of the shallow traps in the film, and thus, these charges are localized. In agreement with this scenario, we note that the PL spectrum of the film and single crystal [Figs. 1(c) and 1(d)] is dominated by an emission band at ~ 2.33 eV that is lower than the obtained E_{exc}, which has excitation fluence (I) dependence in the form of a power law (I)$^\gamma$ [Fig. 1(d) inset] with $\gamma = 1.4$. The value of this exponent $\sim \frac{3}{2}$ and the PL emission energy indicate that the PL emission is due to trap-related electron-hole recombination [16] or trion emission [17].

For measuring the transient QB, we have used ultrafast circularly polarized photoinduced reflectivity (c-PPR) at liquid He temperature, as shown in Fig. 2(b). The experimental setup is a derivative of the well-known degenerate pump-probe technique, where the polarization of the pump beam is modulated by a photoelastic modulator between left (δ^+) and right (δ^-) circular polarization (LCP and RCP, respectively). In this scheme, the probe beam is circularly polarized (either LCP or RCP) by a quarter wave plate. The transient change in the probe reflection $\Delta R_{\delta^-\delta^+}^{\delta^+\delta^+} = R_{\delta^+\delta^+} - R_{\delta^-\delta^+}$ (for c-PPR) is recorded. In contrast to the traditional pump-probe technique in which the pump intensity is modulated and the measured photoreflectivity is proportional to the photoexcitation density N, the c-PPR dynamics is proportional to the population difference between LCP and RCP pump excitation for a fixed LCP probe, where the c-PPR(t) $\propto N_{\delta^+\delta^+} - N_{\delta^-\delta^+}$.

The pump laser pulses, having ~ 150 fs pulse duration at 80 MHZ repetition rate, could be tuned from 470 to 570 nm and were generated by combining the fundamental beam at 775 or 810 nm extracted from the Ti : sapphire laser (Spectra Physics model) with the infrared beams from the optical parametric amplifier onto a barium borate (BBO) type 2 sum frequency generation (SFG) crystal (see method). The laser
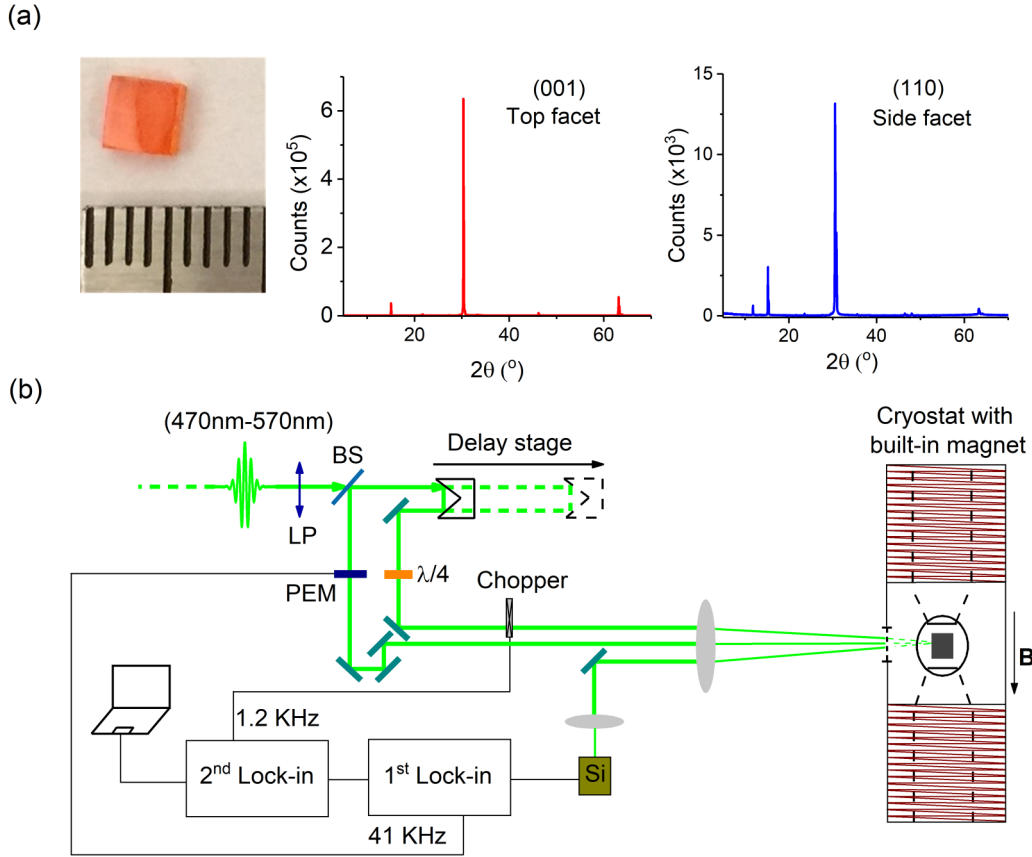
FIG. 2. (a) A picture of the cuboid-shaped $CsPbBr_3$ single crystal with (001) top facet and (110) side facet. (b) X-ray diffraction patterns of (001) and (110) crystal facets. (c) Schematic of the experimental apparatus for degenerate pump-probe transient circularly polarized photoinduced reflection [c-PPR(t)], using two lock-in amplifiers. PEM is a photoelastic modulator for modulating the pump beam polarization between left (δ^+) and right (δ^-) circular polarizations; $\lambda/4$ is a quarter wavelength plate; LP is a linear polarizer; and BS is a beam-splitter. The $CsPbBr_3$ crystal was mounted in a cryostat and cooled down to 4 K. An electromagnet generates a magnetic field **B** up to 700 mT parallel to the crystal surface (Voigt geometry).

beam was split into two beams by an 80/20 beam splitter for the pump and probe in the degenerate configuration. For the nondegenerate case, the 405 nm pump was generated by frequency doubling the fundamental at 810 nm using a second-harmonic generation BBO crystal. These pump-probe beams, having average intensity of ~12 and ~3 W cm^{-2}, respectively, were aligned onto the $CsPbBr_3$ crystal that was placed inside a cryostat with a built-in electromagnet that delivered a field strength B up to 700 mT at temperatures down to 4 K. When measuring the QB at $B = 0$, the c-PPR(t) technique is a unique method for resolving the small exciton fine structure (EFS) splitting, which may be in the microelectronvolt range (with nanosecond oscillatory period). At $B >$ 100 mT, the QB frequencies change linearly with B, from which we obtain the electron and hole g factors.

Our pump-probe PPR measurements were conducted on a $CsPbBr_3$ crystal at 4 K for two crystal facets, namely, (001) and (110) [Fig. 2(a)], with applied magnetic fields parallel to the crystal surface along [010] and [001], respectively. Figure 3 shows the c-PPR(t) dynamics and their corresponding fast Fourier transform (FFT) spectra (Fig. 3 inset) measured for a number of magnetic field strengths at 405 nm pump excitation, which is ~0.73 eV above the band edge of the $CsPbBr_3$ crystal [9]. The probe photon energy was

tuned to be in resonance with the trion peak at ~2.33 eV (533 nm). We can distinguish two beating frequencies in the FFT spectra that increase with increasing B. The two obtained QB frequencies as a function of magnetic field are plotted in Figs. 3(d) and 3(h), respectively, which show linear dependence with the field from which we could obtain their associated g factors. In this case, the fast and slow oscillations correspond to the Larmor precession frequencies of the lone electron in the positive trion T^+ and the lone hole in T^-, respectively [17]. We discard the exciton contribution to the observed QB because (i) the obtained zero-field QB frequency measured on the (001) facet is ~2 μeV [Fig. 4(c)], which is much smaller than the EFS splitting of ~100 μeV in this compound [18,19], and (ii) the QB response of the excitons is predicted to show at least four QB frequencies [17,20], in contrast with the experiment that shows only two QB frequencies. Based on our calculations [15], we attribute the fast oscillation having larger g value to the electron in the positive trion T^+ and the slower oscillation with smaller g value to the hole in the negative trion T^-. From the QB frequencies at large field [Figs. 3(c)–3(f)] measured on the two crystal facets, we obtain the following anisotropic g factors: $|g_{[001]}^{fast}| = |g_{[001]}^e| = 1.95 \pm 0.04$, $|g_{[010]}^{fast}| = |g_{[010]}^e| = 1.82 \pm 0.04$, and $|g_{[001]}^{slow}| = |g_{[001]}^h| = 0.69 \pm 0.02$, $|g_{[010]}^{slow}| = |g_{[010]}^h| = 0.76 \pm$
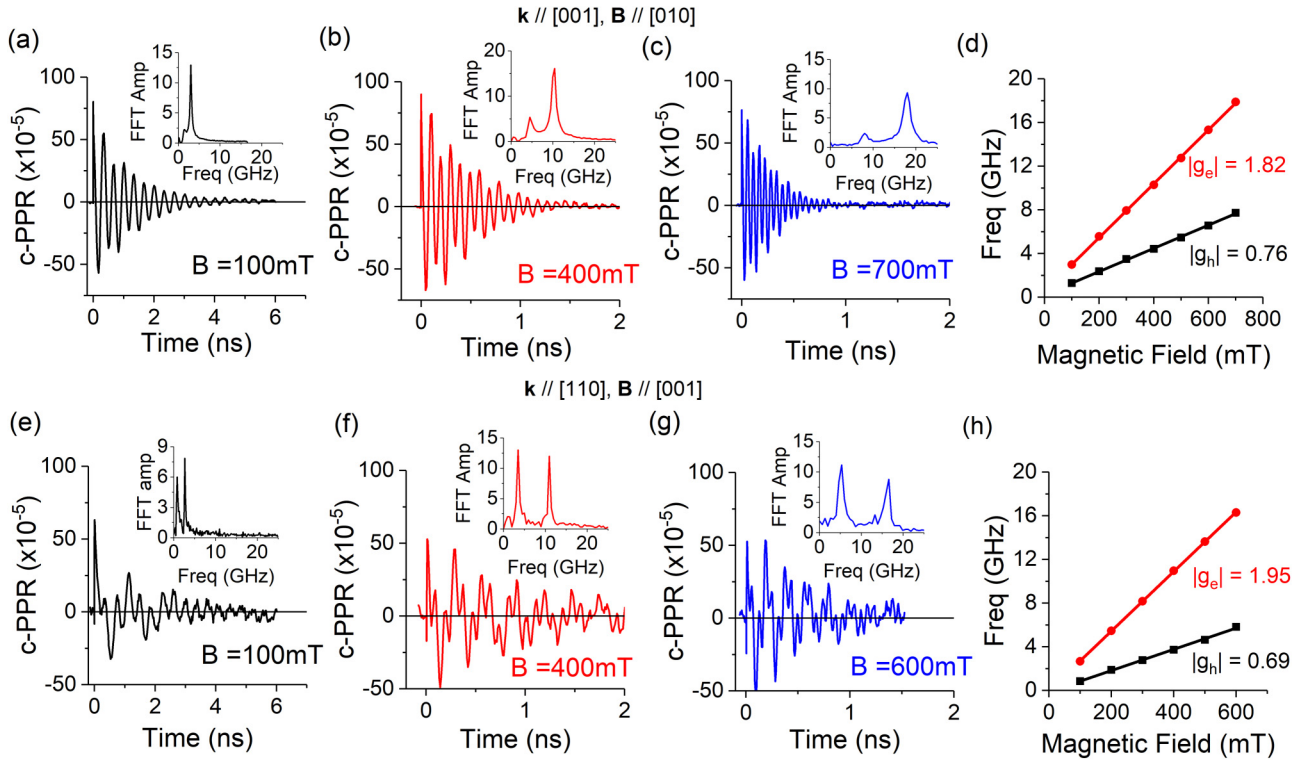
FIG. 3. Photoinduced quantum beatings (QBs) in CsPbBr$_3$ single crystal excited at 405 nm measured at various magnetic field strengths at 4 K. Magnetic field dependence of the transient circularly polarized photoinduced reflection [c-PPR(t)] measured on (a)–(d) the (001) facet with **B** directed along [010] and (e)–(h) the (110) facet with **B** along [001], using probe at 533 nm. The insets show the corresponding fast Fourier transform (FFT) spectra with two FFT peaks for the fast and slow oscillatory frequencies. (d) and (h) Fast and slow QB frequencies vs *B* and the obtained *g* factors.

0.02. These obtained values show that the *g* factors of both electrons and holes are substantially anisotropic in the CsPbBr$_3$ orthorhombic phase. We also measured the QB spatial dependence on the (001) facet at $B = 400$ mT, as shown in Fig. S2 in the Supplemental Material [15]. The QB amplitude depends on the illuminated spot position on the crystal facet, but the QB frequency stays robust at 10.2 GHz within the measurement uncertainty. The anisotropic *g* factors are quantitatively analyzed by applying the 8-band **k·p** model developed for orthorhombic HOIPs [15,17]. From the best fit to the measured *g* factors (see Supplemental Material Fig. S2 [15]), we determine the Kane energy $E_p = 11.05$ eV, the tetragonal and orthorhombic crystal field parameters $\delta = -466.2$ meV, $\zeta = 239.4$ meV, respectively, and Luttinger's magnetic parameter $= -0.24$. In these fits, we used the spin-orbit split-off parameter $\Delta = 1.543$ eV, calculated using the hybrid density functional theory [21], and took the value of the bandgap as 2.34 eV based on the measured exciton energy [see Fig. 1(a)].

It is not possible to determine the sign of g_e and g_h from the QB experiment. To determine the *g*-value polarity, we used the technique of MCD of the excitons in CsPbBr$_3$ thin films for measuring the *g* value of the bright exciton g_{ex} at 4 K. The MCD technique is described elsewhere [22]. For this technique, the different absorption of LCP ($\sigma+$) and RCP ($\sigma+$) light under high magnetic field is recorded in the Faraday geometry. The high magnetic field up to 17.5 T was provided by a superconducting magnet (Maglab SCM cell 3).

The MCD signal is obtained from the relation:

$$\text{MCD} = \frac{[T(\sigma+) - T(\sigma-)]}{[T(\sigma+) + T(\sigma-)]/2}, \quad (1)$$

where $T(\sigma+)$ and $T(\sigma-)$ are the respective optical transmission of LCP and RCP light. In the presence of an external magnetic field applied parallel to the light propagation direction, the two nearly degenerate bright exciton states, *X* and *Y*, in the orthorhombic CsPbBr$_3$ phase are mixed by the magnetic field to form states of opposite angular momentum which are split in energy. This leads to an energy difference ΔE in the absorption of LCP and RCP light that results in a derivativelike MCD spectrum. The relation between the MCD signal and the underlying ΔE can be therefore expressed as

$$\text{MCD} = \frac{d\ln[T(E)]}{dE}\Delta E. \quad (2)$$

In Eq. (2), $\Delta E = g_{ex}\mu_B B$, where μ_B is the Bohr magneton. Figure 5(a) shows the MCD spectra at 4 K measured at various magnetic fields that exhibit a derivativelike feature related to the exciton absorption band in CsPbBr$_3$ [see Fig. 1(a)]. The MCD magnitude (namely, peak value) was plotted as a function of *B* in Fig. 5(b) which shows a linear dependence. We fit the MCD(*B*) dependence using Eq. (2) from which we obtain $g_{exc} = 2.18 \pm 0.08$. The bright exciton *g* value for the orthorhombic phase is related to the *g* values of the electrons and holes as $g_{ex} = g_e + g_h$. From the QB experiment [Fig. 3(d)], we measured $|g_e| = 1.95$ and $|g_h| = 0.69$ for **B**
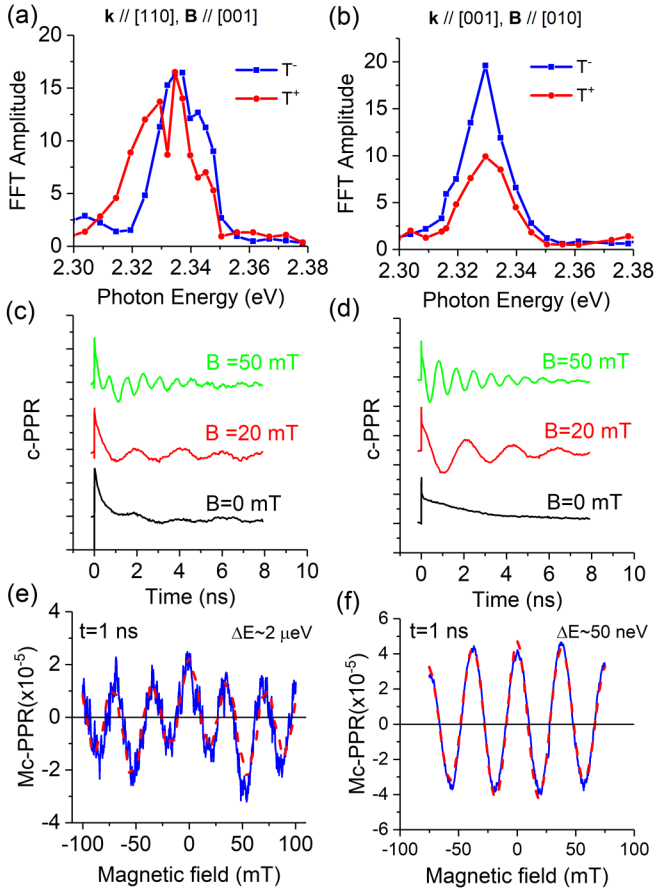
FIG. 4. (a) and (b) Probe beam spectrum of the quantum beating (QB) fast Fourier transform (FFT) amplitude for the fast (blue, T^-) and slow (red, T^+) oscillations measured at $B = 400\,\text{mT}$, excited at 405 nm on (a) the (110) facet with **B** along [001] and (b) the (001) facet with **B** along [010]. Transient circularly polarized photoinduced reflection [c-PPR(t)] dynamics measured at three different fields on (c) the (110) surface with **B** ∥ [001] and (d) (001) with **B** ∥ [010], using 533 nm probe wavelength. Magnetic field response of the c-PPR (Mc-PPR) measured at fixed delay time $\Delta t = 1\,\text{ns}$ on (e) the (110) surface with **B** ∥ [001] and (f) the (001) surface with **B** ∥ [010]. The dashed (red) lines are fits using Eq. (3) with extracted zero-field splitting $\Delta E_{(110)} = 2\,\mu\text{eV}$ and $\Delta E_{(001)} = 50\,\text{neV}$, respectively.
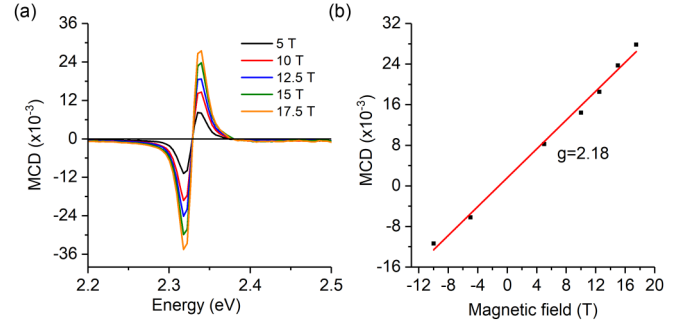

FIG. 5. Magnetic circular dichroism (MCD) of a $CsPbBr_3$ thin film measured at 4 K in the Faraday configuration. (a) MCD spectra obtained at various magnetic fields. (b) MCD peak vs the magnetic fields and the extracted exciton Landé g factor of the exciton $g_{\text{exc}} = 2.18 \pm 0.08$ using a linear fit (red line).

along the z direction. Consequently, to satisfy the relation $g_{\text{ex}} = g_e + g_h$, we conclude that g_h cannot be negative. We thus confirm that $g_h > 0$ for $CsPbBr_3$ [23,24]. In contrast, it has been found that $g_h < 0$ in $MAPbI_3$ [17,20].

To complete our studies, we also measured the QB spectra of the fast and slow oscillations by changing the probe photon energy while keeping the excitation beam wavelength fixed at 405 nm. For these spectra, we considered the peak amplitude of the fast and slow QB frequencies in the FFT spectra (see Fig. 3 inset) and plotted these against the probe photon energy. Figures 4(a) and 4(b) show the QB spectrum measured on two facets of (110) and (001) with the **B** field directed along [001] and [010], respectively. We note that, for **B** along [010], the QB spectra of the fast and slow oscillations peak at the trion energy ~2.33 eV. However, the QB spectrum of **B** along [001] is broadened to both sides of the trion peak.

In contrast with excitons, localized electrons and holes as well as ground state trions do not possess zero-field splitting (ZFS). Consequently, no QB should be observed at $B = 0$. Indeed, in Fig. 4(d), the c-PPR dynamics measured at $B = 0$ on the (001) crystal facet does not show any QB oscillations up to 8 ns. To confirm this, we did a control experiment, where we applied a small field of 20 mT which shows QB oscillation at a frequency of ~500 MHz [see Fig. 4(d)]. This indicates that the maximum ZFS here is of the order of 100 neV, which is three orders of magnitude smaller than the measured EFS of ~100 μeV [18,19]; this supports the interpretation that the QBs originate from localized carriers [9] or trions [17] rather than excitons. However, the c-PPR dynamics measured on the (110) crystal facet exhibits a beating oscillation with a frequency of ~510 MHz (~2 μeV) which in fact does not change up to $B = 20\,\text{mT}$ [Fig. 4(c)]. This ZFS value is still much smaller than the ~100 μeV expected for the exciton [18,19]. We speculate that the ZFS is due to a small field in the sample even when the applied field is null. Recently, it was proposed that the pump and probe beams in the c-PRR experiment even at $B = 0$ cause dynamic nuclear spin polarization via the hyperfine flip-flop process, which in turn gives rise to an Overhauser field B_N [10–12]. In this case, the zero-field beating results from the Zeeman splitting caused by B_N, which we estimate to be on the order of 10 mT, given that $g^e_{[001]} = 1.95$.

For determining the QB frequency at $B = 0$ more accurately, we also measured the magnetic field response of the c-PPR dynamics at fixed delay time, Δt named magnetic c-PPR or Mc-PPR(Δt, B). Specifically, we scanned the magnetic field in an interval from $-B_0$ to $+B_0$ while measuring the c-PPR signal at a fixed delay time Δt. The Mc-PPR technique, namely, resonant spin amplification, was utilized before [25] for measuring the long spin lifetime of resident electrons in inorganic quantum wells that may be longer than the laser repetition time. Figures 4(e)–4(f) show the Mc-PPR($\Delta t = 1\,\text{ns}$) response for two crystal surfaces, namely, (110) and (001). The Mc-PPR(B, Δt) responses exhibit two beating oscillations in the magnetic field domain that correspond to the fast and slow beatings measured in the time domain that originate from the localized electron and hole or trions (Fig. 3). We fitted the observed Mc-PPR(B, Δt) responses with a double
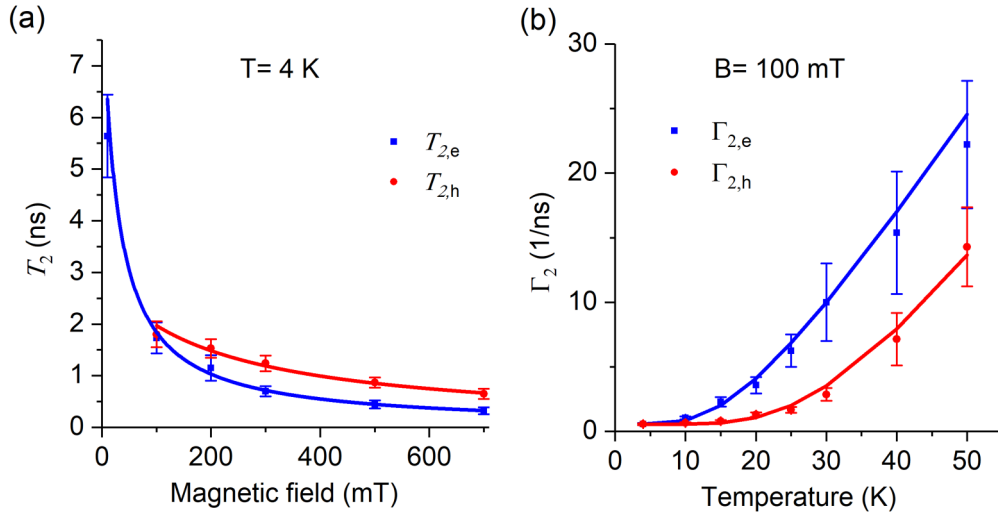
FIG. 6. (a) Spin lifetime of photoinduced electrons (blue squares) and holes (red circles) vs the magnetic field measured at 4 K with **B** along [010], which is extracted from the quantum beating (QB) dynamics [Eq. (4)]. The lines through the data points are fits using Eq. (5). (b) Spin dephasing rate of electrons (blue square) and holes (red circle) as a function of temperatures for $B = 100$ mT. The lines through the data points are fits using Eq. (6).

sum of damped oscillation functions [17,25]:

$$
\begin{aligned}
\text{Mc} &- \text{PPR}(B, \Delta t) \\
&= \sum_n \Theta(\Delta t + n t_{\text{rep}}) \sum_{i=\text{e,h}} A_i \exp[-\Gamma_i(\Delta t + n t_{\text{rep}})] \\
&\quad \times \cos\left[\frac{g_i \mu_B B + \Delta E}{\hbar}(\Delta t + n t_{\text{rep}})\right],
\end{aligned}
\tag{3}
$$

where n represents the present pump pulse and all preceding pump pulses that contribute to the Mc-PPR response. This occurs because the long spin relaxation time leads to spin polarization buildup from previous pump pulses. Note that the laser repetition rate here is 80 MHz, or equivalently $t_{\text{rep}} = 12.5$ ns, whereas the spin lifetime is ~5 ns. Therefore, it is not expected that more than one preceding pulse excitation would contribute the Mc-PPR, or $n = 1$, 2 in Eq. (3). The index i (either 1 or 2) in Eq. (3) represents the electron and hole contributions, where Γ_i and g_i are, respectively, the spin relaxation rate $\Gamma_{\text{e(h)}}$ (that depend linearly on B) and Landé g factors of the electron and hole. In Eq. (3), we also introduced an important fitting parameter, namely, ΔE, which we attribute to the ZFS of the underlying photoexcitons that give rise to the QB oscillation at $B = 0$.

The Mc-PPR responses were fitted by adjusting the two A_i values and ΔE, while taking $g_{\text{e(h)}}$ from the QB at high field (Fig. 3) and the relaxation rates $\Gamma_i(B)$ from Fig. 6(a). A good fit was obtained for both (001) and (110) surfaces with $\Delta E_{(001)} = 50$ neV and $\Delta E_{(110)} = 2\,\mu$eV, respectively [Figs. 4(e) and 4(f)]. Note that the two ΔE values are in excellent agreement with the ZFS extracted from the QB experiment in the time domain at $B = 0$ [Figs. 4(c) and 4(d)].

From the c-PPR dynamics (Figs. 3 and 4), we can obtain the electron and hole spin lifetime by fitting the QB transient response with two damped oscillation functions:

$$
\begin{aligned}
A_1 \exp\left(\frac{-t}{T_{2,\text{e}}}\right) &\cos(2\pi f_1 t + \phi_1) + A_2 \exp\left(\frac{-t}{T_{2,\text{h}}}\right) \\
&\times \cos(2\pi f_2 t + \phi_2),
\end{aligned}
\tag{4}
$$

where $T_{2,\text{e}}$ and $T_{2,\text{h}}$ are the spin dephasing times of the electrons and holes; f_1 and f_2 are the two QB frequencies that can be obtained directly from the FFT of the c-PPR dynamics (Fig. 3). We note that, at $B < 10$ mT, the c-PPR(t) response oscillates beyond 8 ns (Fig. 4), which indicates a very long spin relaxation time in the CsPbBr$_3$ single crystal. In fact, we extracted from the fitting (Fig. 4), $T_{2,\text{e}} = 5.6$ ns for $B = 10$ mT. As depicted in Fig. 6(a), the electron and hole spin relaxation times $T_{2,\text{e}}$ and $T_{2,\text{h}}$ measured on the (001) crystal facet with **B** directed along [010] steeply decrease with B as $1/B$. Previous studies of CdTe quantum wells attributed the $1/B$ dependence of $T_2(B)$ to a dispersion of carrier g factors, Δg caused by an inhomogeneous dephasing of an ensemble of carrier spins (5, 6), which can be described by the relation:

$$
\frac{1}{T_2^*} = \frac{1}{\tau_0} + \frac{\Delta g \mu_B B}{\hbar}.
\tag{5}
$$

Here, $T_2^* = T_{2,\text{e}}$ or $T_{2,\text{h}}$, and τ_0 is the spin lifetime at $B = 0$. We fit the measured $T_2^*(B)$ response using Eq. (5) [see Fig. 6(a)] and obtained $\Delta g_\text{e} = 0.048$ and $\Delta g_\text{h} = 0.019$ for **B** along the [010] crystal orientation.

Furthermore, we found that the spin-relaxation rates for both electrons ($\Gamma_{2,\text{e}}$) and hole ($\Gamma_{2,\text{h}}$) increase with increasing temperature up to 50 K [Fig. 6(b)], which is the highest temperature that we could still observe QB in the CsPbBr$_3$ crystal. The measured $\Gamma_{2,\text{e(h)}}(T)$ response supports the Elliot-Yafet spin-relaxation mechanism which arises from spin-orbit-related scattering collisions with phonons. At high temperature, the phonon occupation number $\langle n \rangle = \frac{1}{\exp\left(\frac{\hbar\omega}{K_B T}\right) - 1}$ increases, which explains the dephasing rate increase. We fit the $\Gamma_{2,\text{e(h)}}(T)$ data using the function:

$$
\Gamma_{2,\text{e(h)}} = \Gamma_0^{\text{e,(h)}} + \Gamma_\omega^{\text{e,(h)}} \frac{1}{\exp\left(\frac{\hbar\omega0}{K_B T}\right) - 1},
\tag{6}
$$

where $\Gamma_0^{e,(h)}$ is the temperature-independent scattering rate from defects and impurities, $\Gamma_\omega^{e,(h)}$ is the scattering rate from phonons, and ω_0 is a typical optical phonon frequency. Good fit for $\Gamma_{2,e}$ (T) and $\Gamma_{2,h}$ (T) was obtained with $\Gamma_0^{e(h)} = 0.52(0.57) \pm 0.1(0.15)\,(1/\text{ns})$, $\Gamma^{e(h)} = 44(120) \pm 3(8)\,(1/\text{ns})$, and $\hbar\omega_0 = 4.5(10) \pm 1(2)$ meV [Fig. 6(b)]. The fact that $\Gamma_0 \ll \Gamma_\omega$ indicates that the carrier scattering with defect/impurity is quite small in this high-quality $CsPbBr_3$ single crystal. The fitting also shows that longitudinal optical phonons with energy <12 meV are the dominant scatterers for the spin-relaxation dynamics in $CsPbBr_3$ [26,27].

[1] M. M. Lee, J. Teuscher, T. Miyasaka, T. N. Murakami, and H. J. Snaith, Efficient hybrid solar cells based on meso-superstructured organometal halide perovskites, Science **338**, 643 (2012).

[2] J. H. Heo, S. H. Im, J. H. Noh, T. N. Mandal, C.-S. Lim, J. A. Chang, Y. H. Lee, H.-J. Kim, A. Sarkar, Md. K. Nareeruddin *et al.*, Efficient inorganic–organic hybrid heterojunction solar cells containing perovskite compound and polymeric hole conductors, Nat. Photonics **7**, 486 (2013).

[3] M. Liu, M. B. Johnston, and H. J. Snaith, Efficient planar heterojunction perovskite solar cells by vapour deposition, Nature (London) **501**, 395 (2013).

[4] H. Zhou, Q. Chen, G. Li, S. Luo, T.-B. Song, H.-S. Duan, Z. Hong, J. You, Y. Liu, and Y. Yang, Interface engineering of highly efficient perovskite solar cells, Science **345**, 542 (2014).

[5] L. Protesescu, S. Yakunin, M. Bodnarchuk, F. Krieg, R. Caputo, C. H. Hendon, R. X. Yang, A. Walsh, and M. V. Kovalenko, Nanocrystals of cesium lead halide perovskites ($CsPbX_3$, $X =$ Cl, Br, and I): Novel optoelectronic materials showing bright emission with wide color gamut, Nano Lett. **15**, 3692 (2015).

[6] J. Maes, L. Balcaen, E. Drijvers, Q. Zhao, J. D. Roo, A. Vantomme, F. Vanhaecke, P. Geiregat, and Z. Hens, Light absorption coefficient of $CsPbBr_3$ perovskite nanocrystals, J. Phys. Chem. Lett. **9**, 3093 (2018).

[7] S. Yuan, Z.-K. Wang, M.-P. Zhuo, Q.-S. Tian, Y. Jin, and L.-S. Liao, Self-assembled high quality $CsPbBr_3$ quantum dot films toward highly efficient light-emitting diodes, ACS Nano **12**, 9541, (2018).

[8] Y. Feng, H. Wei L.Pan, Y. Liu, Z. Ni, J. Zhao, P. N. Rudd, L. R. Cao, and J. Huang, Low defects density $CsPbBr_3$ single crystals grown by an additive assisted method for gamma-ray detection, J. Mater. Chem. C **8**, 11360 (2020).

[9] V. V. Belykh, D. R. Yakovlev, M. M. Glazov, P. S. Grigorzev, M. Hussain, J. Rautert, D. N. Dirin, M. V. Kovalenko, and M. Bayer, Coherent spin dynamics of electrons and holes in $CsPbBr_3$ perovskite crystals, Nat. Comm. **10**, 673 (2019).

[10] E. Kirstein, D. R. Yakovlev, M. M. Glazov, E. Evers, E. A. Zhukov, V. V. Belykh, N. E. Kopteva, D. Kudlacik, O. Nazarenko, D. N. Dirin, M. V. Kovalenko, and M. Bayer, Lead-dominated hyperfine interaction impacting the carrier spin dynamics in halide perovskites, Adv. Mater. **34**, 2105263 (2022).

[11] D. Paget, G. Lampel, B. Sapoval, and V. I. Safarov, Low field electron-nuclear spin coupling in gallium arsenide under optical pumping conditions, Phys. Rev. B **15**, 5780 (1976).

[12] C. W. Lai, P. Maletinsky, A. Badolato, and A. Imamoglu, Knight-Field-Enabled Nuclear Spin Polarization in Single Quantum Dots, Phys. Rev. Lett. **96**, 167403 (2006).

[13] Y. Yang, D. P. Ostrowski, R. M. France, K. Zhu, J. V. D. Lagemaat, J. M. Luther, and M. Beard, Observation of a hot-phonon bottleneck in lead-iodide perovskites, Nat. Photonics **10**, 53 (2016).

[14] R. J. Elliott, Intensity of optical absorption by excitons, Phys. Rev. **108**, 1384 (1957).

[15] See Supplemental Material at http://link.aps.org/supplemental/10.1103/PhysRevB.106.094306 for FTIR PA method, theoretical calculation of the *g* factors, supplemental figures and tables, and sample preparation, which includes Refs. [28–32].

[16] M. Saba, M. Cadelano, D. Marongiu, F. Chen, V. Sarritzu, N. Sestu, C. Figus, M. Aresti, R. Piras, A. G. Lehmann *et al.*, Correlated electron–hole plasma in organometal perovskites, Nat. Comm. **5**, 5049 (2015).

[17] U. N. Huynh, Y. Liu, A. Chanana, D. R. Khanal, P. C. Sercel, J. Huang, and Z. V. Vardeny, Transient quantum beatings of trions in hybrid organic tri-iodine perovskite single crystal, Nat. Comm. **13**, 1428 (2022).

[18] M. A. Becker, R. Vaxenburg, G. Nedelcu, P. C. Sercel, A. Shabaev, M. J. Mehl, J. G. Michopoulos, S. G. Lambrakos, N. Bernstein, J. L. Lyons *et al.*, Bright triplet excitons in caesium lead halide perovskites, Nature (London) **553**, 189 (2018).

[19] M. Baranowski, K. Galkowski, A. Surrente, J. Urban, Ł. Kłopotowski, S. Maćkowski, D. K. Maude, R. B. Aich, K. Boujdaria, M. Chamarro *et al.*, Giant fine structure splitting of the bright exciton in a bulk MAPbBr$_3$ single crystal, Nano Lett. **19**, 7054 (2019).

[20] P. Odenthal, W. Talmadge, N. Gundlach, R. Wang, C. Zhang, D. Sun, Z.-G. Yu, Z. V. Vardeny, and Y. S. Li, Spin-polarized exciton quantum beating in hybrid organic–inorganic perovskites, Nat. Phys. **13**, 894 (2017).

[21] P. C. Sercel, J. L. Lyons, N. Bernstein, and A. L. Efros, Quasicubic model for metal halide perovskite nanocrystals, J. Chem. Phys. **151**, 234106 (2019).

[22] C.-H. Huang, H.-S. Hsu, S.-J. Sun, Y.-Y. Chang, P. Misiuna, and L. T. Baczewski, Extraction of magnetic circular dichroism effects from blended mixture of magnetic linear dichroism signals in the cobalt/Scotch tape system, Sci. Rep. **9**, 17192 (2019).

[23] E. Kirstein, D. R. Yakovlev, M. M. Glazov, E. A. Zhukov, D. Kudlacik, I. V. Kalitukha, V. F. Sapega, G. S. Dimitriev, M. A. Semina, M. O. Nestoklon *et al.*, The Landé factors of electrons and holes in lead halide perovskites: universal dependence on the band gap, Nat. Comm. **13**, 3062 (2022).

[24] L. M. Jacoby, M. J. Crane, and D. R. Gamelin, Coherent spin dynamics in vapor-deposited $CsPbBr_3$ perovskite thin films, Chem. Mater. **34**, 1937 (2022).

[25] J. M. Kikkawa and D. D. Awschalom, Resonant Spin Amplification in *n*-Type GaAs, Phys. Rev. Lett. **80**, 4313 (1998).

[26] C. M. Iaru, J. J. Geuchies, P. M. Koenraad, D. Vanmaekelbergh, and A. Y. Silov, Strong carrier-phonon coupling in lead halide perovskite nanocrystals, ACS Nano **11**, 11024 (2017).

[27] C. C. Stoumpos, C. D. Malliakas, J. A. Peters, Z. Liu, M. Sebatian, J. Im, T. C. Chasapis, A. C. Wibowo, D. Y. Chung, A. J. Freeman *et al.*, Crystal growth of the perovskite semiconductor $CsPbBr_3$: A new material for high-energy radiation detection, Cryst. Growth Des. **13**, 2722 (2013).

[28] J. Even, L. Pedesseau, J.-M. Jancu, and C. Katan, Importance of spin-orbit coupling in hybrid organic/inorganic perovskites for photovoltaic applications, J. Phys. Chem. Lett. **4**, 2999 (2013).

[29] Z. G. Yu, Effective-mass model and magneto-optical properties in hybrid perovskites, Sci. Rep. **6**, 28576 (2016).

[30] J. Even, L. Pedesseau, C. Katan, M. Kepenikian, J.-S. Lauret, D. Sapori, and E. Deleporte, Solid-state physics perspective on hybrid perovskite semiconductors, J. Phys. Chem. C **119**, 10161 (2015).

[31] J. M. Luttinger, Quantum theory of cyclotron resonance in semiconductors: general theory, Phys. Rev. **102**, 1030 (1956).

[32] P.-O. Lowdin, A note on the quantum-mechanical perturbation theory, J. Chem. Phys. **19**, 1396 (1951).